ADVANCED FUNCTIONAL MATERIALS
www.afm-journal.de

Crosstalk-Free Dual-Band Detection of Visible and Near-Infrared Light Enabled by the Combination of Optical Design and One-Step Transfer Printing

Haijun Jiang, Yuanhong Hu, Xinwen Gao, Tongzhou Wei, Ning Li, Qiaoming Zhang, Weiyao Jia, Lixiang Chen, Xiaotong Guo,* and Yanlian Lei**

Eliminating optical crosstalk in multi-band photodetectors is crucial for effective signal differentiation across wavelengths, particularly in optical communication and bioimaging applications. This study presents a strategy for achieving crosstalk-free dual-band organic photodetectors (OPDs) that integrate broadband visible and narrowband near-infrared (NIR) detection. A back-to-back structure combining a visible detector and a NIR detector is employed using a one-step transfer printing process. The front visible detector is designed for sensing visible photons, while the rear NIR detector is dedicated to detecting NIR photons. The transfer printing technique allows for an increased thickness of the rear NIR light-absorbing layer, efficiently filtering out unwanted visible light. This design not only optimizes light distribution but also manipulates the charge collection, yielding a crosstalk-free dual-band OPD with peak responsivities of 115.0 mA W^{-1} at 450 nm for visible detection and 85.5 mA W^{-1} at 780 nm for NIR detection with a full width at half maximum of 47 nm. The device demonstrates robust performance in anti-interference optical communication, accurately distinguishing target signals amidst multiple interferences. These findings pave the way for future advancements in optical crosstalk-free multi-band photodetector.

1. Introduction

Organic photodetectors (OPDs) are promising candidates to compensate for conventional inorganic optical detection technologies due to their customizable optical and electronic properties, flexibility, and suitability for large-area, solution-based processing.[1–3] Unlike inorganic counterparts, OPDs can achieve narrow-band light responses without the need for external filters.[4] Various filter-free techniques, including optical microcavities,[5,6] narrowband absorbing materials,[7,8] charge collection narrowing (CCN),[4,9–11] charge injection narrowing,[12–15] and exciton dissociation narrowing[16,17] have been developed. These narrowband detection techniques also facilitate the design of cost-effective dual-band OPDs through vertical stacking of different photosensitive units.[18–21]

The dual-band photodetectors are particularly suitable for applications in environmental monitoring, bioimaging, security, and machine vision, as they enable the detection of distinct spectral bands.[22–32] Recent advancements include the development of dual-mode OPDs capable of detecting both near-infrared (NIR) and visible light within a single device.[19] The same method also enables the extension of the dual-band detector to respond to blue, green, and red light.[29] Furthermore, these dual-mode detectors can utilize various semiconductor material systems, such as organic semiconductors, perovskites, and quantum dots,[20–23,33] showcasing their significant potential for practical applications. However, a critical challenge persists in existing dual-band OPDs: the inter-band crosstalk, i.e., the overlap between the two detection bands, adversely affects detection accuracy in applications like image recognition and optical communication.

In this study, we present a strategic approach to eliminate optical crosstalk in typical dual-band OPDs with a vertical back-to-back stacking structure. This design places the heterojunction for short-wavelength (visible light) absorption at the front side and the heterojunction for long-wavelength (NIR light) absorption at the rear side. Different from the previous approaches such as increasing the thickness of the front unit[18–20,34] or adding an optical spacer,[19] we chose to increase the thickness of the rear NIR absorbing layer using a one-step transfer printing method. This technique not only overcomes the limitations of preparing thick films on existing organic layers via solution methods but also realizes the crosstalk-free photoresponse in dual-band

H. Jiang, Y. Hu, X. Gao, T. Wei, W. Jia, L. Chen, Y. Lei
School of Physical Science and Technology
Chongqing Key Lab of Micro&Nano Structure Optoelectronics
Southwest University
Chongqing 400715, China
E-mail: yllei@swu.edu.cn

N. Li, Q. Zhang
School of Electronic and Optical Engineering
Nanjing University of Science and Technology
Nanjing, Jiangsu 210094, China
E-mail: nl@njust.edu.cn

X. Guo
Chongqing CEPREI Industrial Technology Research Institute Co., Ltd.
Chongqing 401332, China
E-mail: guoxiaotong@ceprei.com

The ORCID identification number(s) for the author(s) of this article can be found under https://doi.org/10.1002/adfm.202500628

DOI: 10.1002/adfm.202500628

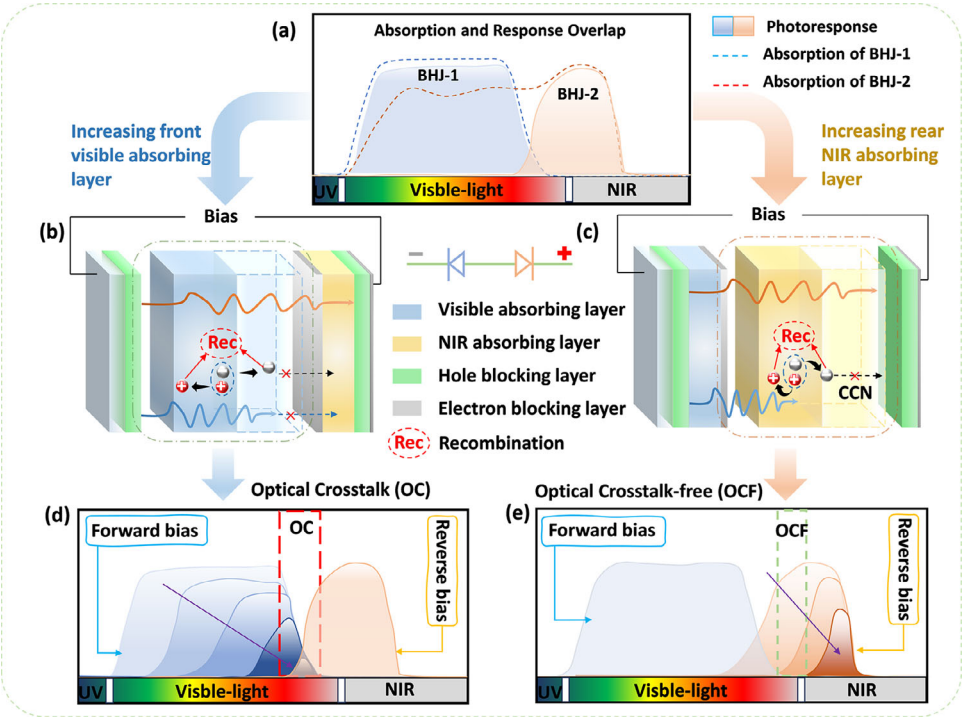

Figure 1. Schematic illustration of the OCF-OPD working mechanism. a) Overlap of absorption and response between the two subcells in a typical dual-mode OPD. Effects of increasing the thickness of b) the front visible absorbing layer and c) the rear NIR absorbing layer. d,e) Corresponding changes in photoresponse with varying thickness of the front visible absorbing layer and rear NIR absorbing layer. Arrows indicate increasing thickness. The optical crosstalk (OC) and optical crosstalk-free (OCF) parts are indicated.

detectors. This is accomplished by effectively filtering out unwanted short-wavelength light through optimized light distribution and selective CCN within the device. The resulting dual-band OPDs effectively detect visible light under forward bias and narrowband NIR light under reverse bias without optical crosstalk. More importantly, this approach is broadly applicable, eliminating the need for careful selection or design of the absorbing layers. The successful implementation of these dual-band OPDs for anti-interference signal detection and optical communication provides valuable insights for developing future multi-mode photodetectors devoid of inter-band crosstalk.

2. Results and Discussion

2.1. Principle of Optical Crosstalk-Free Dual-Band OPDs

The operational mechanism of dual-band OPDs with a back-to-back stacking structure is illustrated in Figure S1 (Supporting Information). In the conventional NIR/visible dual-band detector, the wide bandgap visible absorbing layer is positioned at the front (near the light incident end), while the long-wavelength NIR absorbing layer is at the rear (far from the light incident end). Under forward bias, carriers generated by visible light in the visible absorbing layer move toward respective electrodes, whereas NIR-generated carriers in the NIR absorbing layer encounter a high energy barrier, resulting in non-radiative recombination losses (Figure S1a,c, Supporting Information). Conversely, under reverse bias, NIR-generated carriers in the NIR absorbing layer are collected, while visible light-induced carriers in the visible absorbing layer experience recombination losses. This configuration enables visible light detection under forward bias and NIR detection under reverse bias,[19,22] ensuring distinct operational modes. However, the front visible absorbing layer usually has limited short-wavelength light absorption, allowing some visible light to pass through to the NIR layer, which causes unwanted optical crosstalk and interference (**Figure** 1a).

Two promising paths are expected to address this issue: (i) increasing the thickness of the front wide-bandgap visible absorbing layer to ensure complete absorption of visible light (Figure 1b); or (ii) enhancing the thickness of the rear narrow-bandgap NIR absorbing layer to narrow the NIR response band by manipulate the charge collection (Figure 1c). We then evaluated two comparative dual-band OPDs: one with an adjustable thickness for the visible absorbing layer while keeping a fixed NIR layer thickness (reference OPD), and another with an adjustable NIR layer thickness while maintaining a fixed visible layer thickness (test OPD). The visible absorbing layer comprised an organic bulk heterojunction (BHJ) of P3HT:PC_{61} BM, while the NIR absorbing layer utilized PTB7-Th:PC_{71} BM BHJ, where P3HT, PTB7-Th, PC_{61} BM, PC_{71} BM are poly(3-hexylthiophene-2,5-diyl), poly[4,8-bis(5-(2-ethylhexyl) thiophen-2-yl)benzo[1,2-b;4,5-b′] dithiophene-2,6-diyl-alt-(4-(2-ethylhexyl)-3-fluorothieno [3,4-b] thiophene)-2-carboxylate-2-6-diyl)], [6,6]-phenyl-C61 butyric acid methyl ester, and [6,6]-phenyl-C71 butyric acid methyl ester, respectively.

The absorption spectra for both layers, shown in Figure S2 (Supporting Information), demonstrate that absorption increases with layer thickness and exhibits a slight red shift,

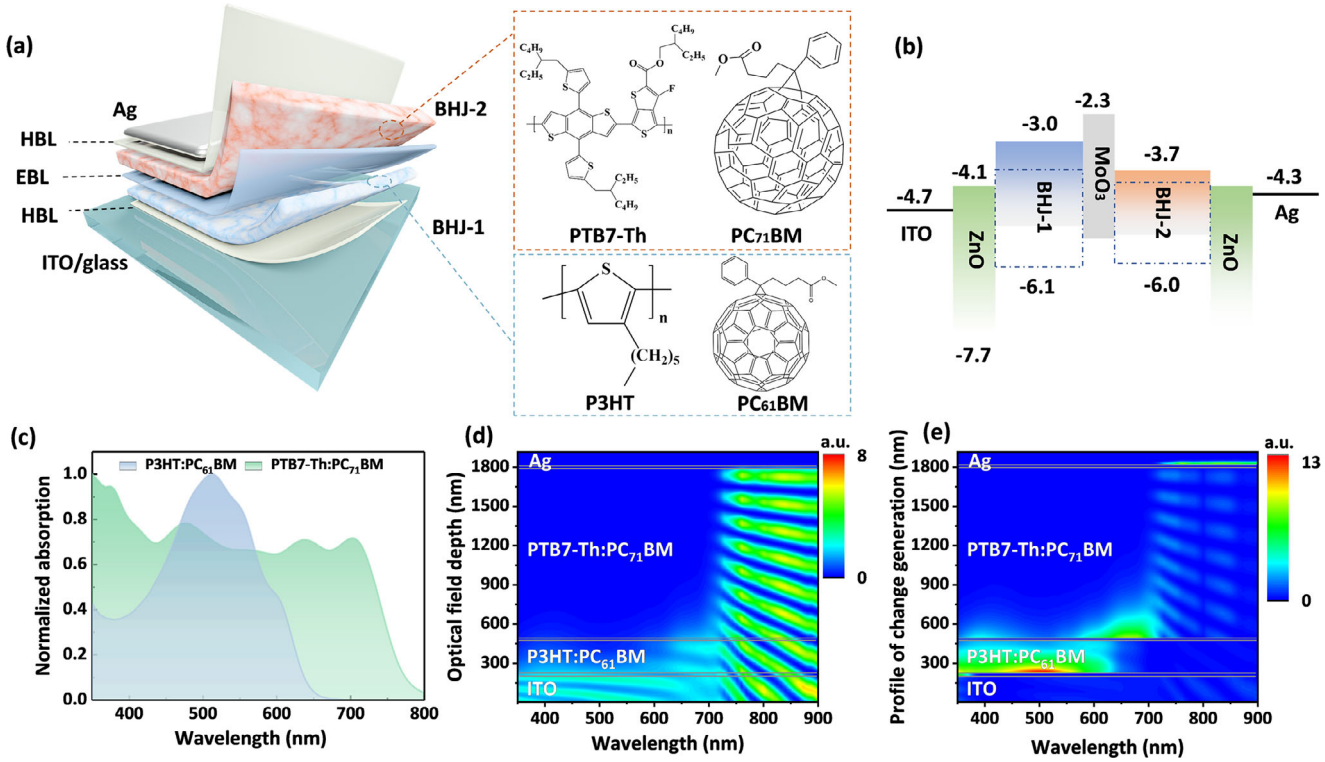

Figure 2. a) Device configuration and optical design of the OCF-OPD. a) Device architecture and the chemical structures of the photosensitive materials used in the two BHJs. b) Schematics of energy level alignment of the functional layers. c) Absorption spectra of the two organic BHJs. d) Simulated optical field distribution and e) charge generation profile in the OCF-OPD.

highlighting the critical role of thickness in determining the absorption coefficient. In the reference, OPD, the external quantum efficiency (EQE) in the short-wavelength range (350–600 nm) decreases with increasing thickness of the visible absorbing layer due to the CCN effect[10,11] under forward bias (Figure S3a, Supporting Information). When the thickness of the front visible absorbing layer reaches 870 nm, the EQE in the range below 600 nm drops to zero. Under reverse bias, the self-filtering effect of the visible layer leads to a gradual decline in EQE in the visible region as the thickness increases, eventually reaching zero (Figure S3b, Supporting Information). Meanwhile, the EQE from the rear NIR layer in the long-wavelength range (600–800 nm) remains unaffected, resulting in significant optical crosstalk near the absorption edge (600–700 nm) of the front layer (Figure 1d). Further increasing the front layer thickness shifts the detection capability from visible/NIR dual-band to NIR single-band.

In contrast, increasing the rear NIR absorbing layer thickness from 232 to 1300 nm in test OPDs causes only minor changes in the response to the short-wavelength band (350–700 nm) under forward bias, while significant changes occur under reverse bias (Figure S3c,d, Supporting Information). This adjustment achieves narrow-band detection near the absorption edge of the rear light absorbing layer in the NIR region (740–840 nm) with a full width at half maximum (FWHM) of less than 50 nm. These findings indicate that enhancing the rear NIR layer thickness further filters out unabsorbed visible light and narrows charge collection, thereby minimizing inter-band crosstalk since the absorption edges of the front and rear BHJ are far apart, and allowing distinct operational modes for visible and NIR detection (Figure 1e).

2.2. Fabrication and Optical Properties of the Crosstalk-Free Dual-Band OPDs

The full structure of the optical crosstalk-free (OCF) visible/NIR dual-band OPD is ITO/ZnO (HBL)/P3HT:PC_{61} BM (2:1)/MoO_3 (EBL)/PTB7-Th:PC_{71} BM (1:1)/ZnO (HBL)/Ag (**Figure 2a**), where HBL, EBL, and MoO_3 are hole blocking layer, electron-blocking layer, and molybdenum trioxide, respectively. The chemical structures of the materials used are displayed in the insets in Figure 2a. Figure 2b presents the energy level diagram of the device, with the energy level values of the materials sourced from the literature.[18,30,35,36] The absorption spectra of the two organic BHJs show complete overlap in the visible range (350–680 nm), as depicted in Figure 2c. The P3HT:PC_{61} BM (BHJ-1) at the front enhances the device's response to visible light by efficiently absorbing relatively high-energy photons. Additionally, this BHJ-1 also acts as a built-in filter for the rear PTB7-Th:PC_{71} BM cell (BHJ-2),[30,34] improving spectral selectivity and optimizing device performance.

To elucidate the unique optoelectronic properties of the optical crosstalk-free dual-band OPD (OCF-OPD), the distribution of the optical field and photogenerated charges were calculated by using the transfer matrix analysis.[19] The simulation results show that the optical field distribution aligns with the charge generation

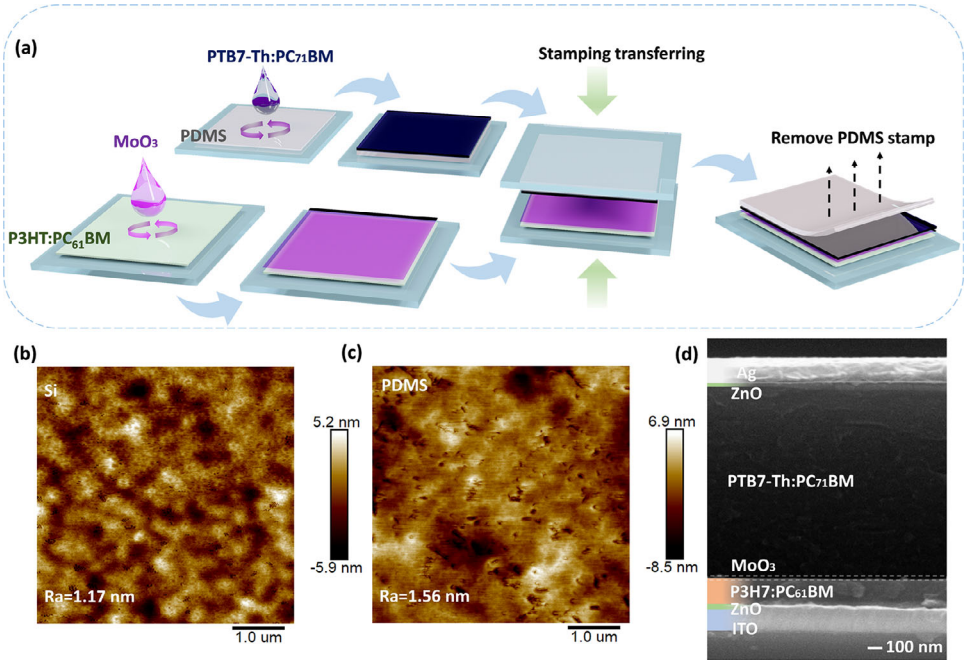

Figure 3. Fabrication of the OCF-OPDs. a) Schematic diagram of the one-step transfer printing process for thick PTB7-Th:PC_{71} BM film using a PDMS stamp. AFM images of spin-coated PTB7-Th:PC_{71} BM film on b) silicon wafer and c) PDMS stamp. d) Cross-section SEM image of the resulting OCF-OPD.

profile, which corresponds to the absorption spectra. As shown in Figure 2d, incident light in the 300–600 nm range is primarily absorbed by the front P3HT:PC_{61} BM BHJ, while light in the 700–900 nm range is absorbed by the rear PTB7-Th:PC_{71} BM BHJ. Moreover, light in the 700–900 nm range penetrates the entire rear PTB7-Th:PC_{71} BM BHJ, generating carriers throughout the rear cell. This characteristic ensures a response to NIR light under reverse bias voltage as the thickness increases. Notably, in the 600–700 nm interval, the reduced absorption capacity of the front P3HT:PC_{61} BM BHJ results in photo-generated carriers in both layers (Figure 2e), leading to the spectral crosstalk that is typically observed in conventional dual-band OPDs (Table S1, Supporting Information). To address this issue, we designed micron-scale rear PTB7-Th:PC_{71} BM BHJs that effectively manipulate carrier transmission and collection, thereby eliminating inter-band optical crosstalk.

However, fabricating micron-scale polymer films using conventional spin-coating methods poses significant challenges, particularly when applied over existing organic layers due to limitations in film thickness and uniformity. To overcome these challenges, we employed a one-step transfer printing method utilizing pre-cleaned polydimethylsiloxane (PDMS). This innovative technique enables the transfer of the PTB7-Th:PC_{71} BM blend onto a MoO_3 substrate, as shown in **Figure** 3a. A key advantage of this method is its ability to produce films with double or triple the thickness of those made through traditional spin-coating, all while maintaining the same solution concentration.

To assess film quality, we conducted atomic force microscopy (AFM) imaging on PTB7-Th:PC_{71} BM films deposited on both silicon wafer and PDMS under identical conditions, revealing mean surface roughness values of 1.17 and 1.56 nm, respectively (Figure 3b,c). These results indicate that the film quality on PDMS is comparable to that on silicon wafers. Figure 3d presents the scanning electron microscopy (SEM) cross-sectional image of the complete device structure, showcasing the effective layering achieved through our method. The one-step PDMS transfer technique not only addresses the challenges of fabricating thicker films but also avoids solution miscibility issues often encountered in multilayer film preparation using alternative methods. This innovation significantly enhances the feasibility and effectiveness of developing high-performance OCF-OPDs.

2.3. Spectral Response Behaviors of the Crosstalk-Free Dual-Band OPDs

Figure 4a shows the current density-voltage (*J-V*) characteristics of the OCF-OPD in dark conditions and under visible (450 nm) or NIR (780 nm) illumination. At a bias of 2 V, the dark current density was $\approx 3.48 \times 10^{-7}$ A cm^{-2}, and $\approx 4.17 \times 10^{-8}$ A cm^{-2} at −2 V. These low dark currents, observed under both forward and reverse bias, are attributed to the sufficiently thick semiconductor films that minimize leakage current and the back-to-back configuration of the BHJs that inhibit external current injection. Notably, significant photocurrent was generated under forward bias (0 to 4 V) in the presence of visible light and under reverse bias (0 to −4 V) with NIR light, highlighting the unique capability for dual-band detection. The EQE spectra, presented in Figure 4b,c, confirm distinct detection bandwidths: 350–680 nm (visible light) under forward bias and 740–900 nm (NIR light) under reverse bias. The combined EQE curves in Figure S4a (Supporting Information) show minimal overlap between these ranges, indicating negligible optical crosstalk.

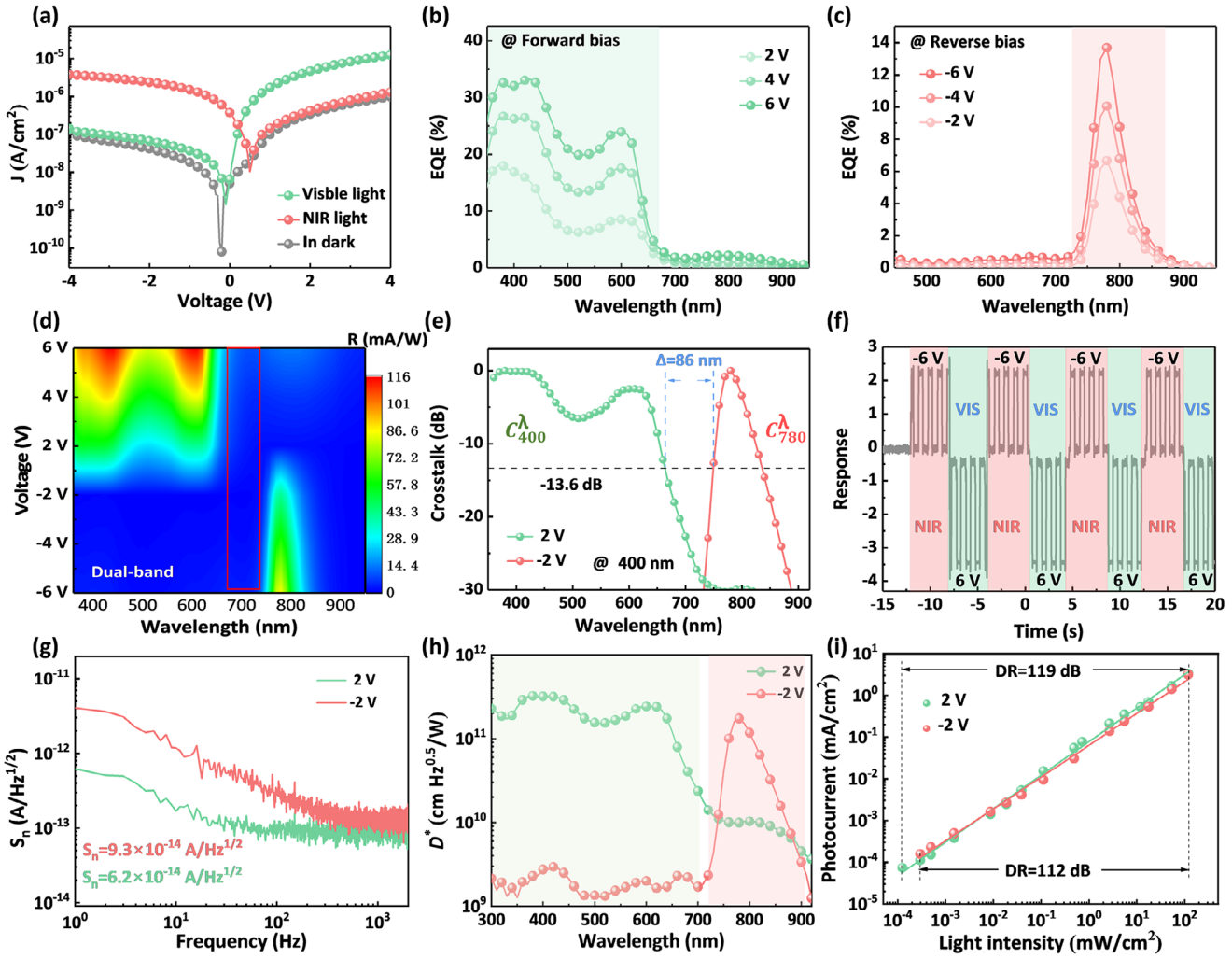

Figure 4. Photoresponse characteristics of the OCF-OPDs. a) *J-V* curves of the OCF-OPDs in dark and under illumination with visible light (450 nm) and NIR (780 nm) at an intensity of 0.16 mW/cm^2. EQE spectra for b) forward bias (visible detection) and c) reverse bias (NIR detection). d) Contour map showing the responsivity of the OCF-OPD as a function of wavelength and bias. e) Spectral crosstalk between the visible (400 nm) and NIR (780 nm) detection bands. f) Photoresponses at ±6 V under 1 Hz-modulated visible and NIR light. g) Noise spectral density, h) specific detectivity (***D****), andx i) dynamic range of the OCF-OPD measured at ±2 V biases.

The optical crosstalk-free detection is further validated by the bias-tunable responsivity (***R***) results. Figure 4d displays the contour map of ***R*** values as a function of wavelength and bias voltage. Under a forward bias of 6 V, the device achieved a peak ***R***-value of 115.0 mA W^{-1} at a wavelength of 450 nm. In reverse bias mode at −6 V, the peak ***R***-value was 85.5 mA W^{-1} at 780 nm. These high responsivity levels are significant given the micrometer-scale absorption layer, especially when compared to conventional non-gain dual-band OPDs (Table S1, Supporting Information). The NIR detection mode also exhibited narrow-band capabilities, with an FWHM of ≈47 nm (Figure S4b, Supporting Information). Notably, a clear gap in responsivity between the visible and NIR detection bandwidths is evident in the red square area of Figure 4d.

To quantitatively evaluate the optical crosstalk in the dual-band OPDs, we calculate the spectral crosstalk by identifying the maximum responsivity values in the NIR and visible spectral bands as the target wavelengths. The spectral crosstalk is defined by[37]

$$C\frac{\lambda}{\lambda_0}\left(V_i\right) = -20 \times \left|\log \frac{R\left(\lambda, V_i\right)}{R\left(\lambda_0, V_i\right)}\right| \quad (1)$$

where $R(\lambda, V_i)$, $R(\lambda_0, V_i)$ represent the responsivity at untargeted and target wavelengths under applied bias V_i. For instance, $C^{\lambda}_{Vis}(2V)$ indicates the crosstalk between visible light and other detection bands at 2 V. As shown in Figure 4e, the $C^{\lambda}_{400}(2V)$ remains below −10 dB in the visible region (390–650 nm), indicating indistinguishable responses and a broadband response in this range (green dot-line). It rapidly decreases to −30 dB in the NIR range, confirming no response in that region. Conversely, $C^{\lambda}_{780}(-2V)$ (crosstalk between 780 nm and other detection spectral bands) remains below −30 dB across the entire visible range (red dot-line), demonstrating narrow-band and visible-blind NIR

detection. In general, crosstalk is negligible when the crosstalk value is larger than −13.6 dB.[38,39] Thus, the wavelength gap (**h**) at this threshold quantitatively characterizes the degree of optical crosstalk: h<0 indicates significant optical crosstalk, while h>0 signifies crosstalk-free conditions. A larger |h| corresponds to a greater degree of overlap (h<0) or dispersion (h>0). As illustrated in Figure 4e, the wavelength gap between the visible and NIR spectral bands is determined to be 86 nm, signifying excellent independence between the spectral response bands. The detection independence is well preserved for target wavelengths of blue (470 nm), green (530 nm), and red (620 nm) (Figure S5, Supporting Information). Additionally, this gap (***h***) remains consistent across varying bias voltages (Figures S5, S6, Supporting Information). Unlike strategies that rely on increasing the front BHJ-1 thickness (h<0, as shown in Figure S7, Supporting Information), the method proposed here effectively eliminates optical crosstalk by increasing the thickness of the rear BHJ-2 (Figure S8, Supporting Information), readily achieving a crosstalk-free dual-band OPD.

The crosstalk-free dual-band detection capability was further demonstrated by operating the device under a ±6 V bias with illumination from frequency-modulated visible (450 nm) and NIR (780 nm) LEDs. As shown in Figure 4f, the device responded solely to 780 nm light under reverse bias and to 450 nm light under forward bias, showcasing its selective dual-band detection capability. The device maintained a stable response after multiple voltage switching cycles, indicating excellent operational stability.

To further illustrate the overall performance of OCF-OPDs, the specific detectivity (***D****) was calculated based on responsivity and noise equivalent power, as follows:[40,41]

$$D^* = \frac{R\sqrt{A}}{S_n} \tag{2}$$

where A and S_n are the device active area (3 × 3 mm^2) and the noise spectral density in $A/Hz^{1/2}$, respectively. The noise spectral density was measured using a Fast Fourier Transform spectrum analyzer under ±2 V bias, as shown in Figure 4g. The results indicate that at frequencies near 1 kHz, S_n levels were below 10^{-13} $A/Hz^{1/2}$ under both forward and reverse bias, attributed to the high film quality and low dark current. As a result, the calculated D^* values for the dual-band OPDs under ±2 V bias close to 10^{11} Jones in their respective detection bands (Figure 4h), and show the absence of optical crosstalk.

The response speed was evaluated by measuring the current response to frequency-modulated illumination at 2 kHz, as shown in Figure S9 (Supporting Information). Under forward bias with 450 nm light illumination, the device exhibited a rise time (τ_{rise}) of 25.6 µs and a fall time (τ_{fall}) of 37.4 µs, while under reverse bias with 780 nm NIR illumination, τ_{rise} was 22.4 µs and τ_{fall} was 32.6 µs, respectively. This fast response speed is comparable to most dual-mode OPDs (Table S1, Supporting Information). Moreover, the device demonstrated a dynamic range close to 6 orders of magnitude (Figure 4i), reaching 119 dB and 112 dB for visible (2 V) and NIR (−2 V), respectively.

To validate the broad applicability of the OCF-OPD structure, we tested various material combinations, including PTB7-Th:PC_{71} BM (BHJ-1) and PTB7-Th:Y6 (BHJ-2), where Y6 is a typical non-fullerene acceptor.[42] Each BHJ exhibited distinct absorption cutoffs (820 nm for BHJ-1 and 950 nm for BHJ-2) while maintaining low dark currents and high detection currents (Figure S10, Supporting Information). Notably, the device demonstrated optical crosstalk-free detection between the visible and NIR bands, with peak responsivities of 130.0 mA W^{-1} at 450 nm and 35.0 mA W^{-1} at 890 nm. The low noise current further enhances the device's performance. These results indicate that the OCF-OPD can effectively utilize various absorption materials for optical crosstalk-free detection without requiring meticulous selection or design of the absorption layers.

2.4. Anti-Interference Optical Communication Applications

The OCF-OPD exhibits exceptional features, including dual-band detection and rapid photoresponse speed, which are essential for identifying target signals amidst multiple inputs in anti-interference optical communications. Figure S11 (Supporting Information) shows the schematic setup for anti-interference signal detection, where multiple light sources of varying wavelengths are integrated to simultaneously generate different signals. The OCF-OPD functions as the receiver, with a silicon photodetector (Si PD) serving as a reference, effectively identifying and responding to target signals from various inputs (different waveforms, duty cycles, and frequencies) with the support of a signal amplifier and an oscilloscope. Specifically, blue (450 nm), green (534 nm), red (652 nm), NIR (780 nm), and short-wave infrared (SWIR, 1050 nm) LEDs were employed as light sources. The frequency, waveform, and duty cycle of each light source were modulated by the signal generator, with the NIR signal (780 nm) designated as the target and the others as interference. As shown in **Figure 5a**, when the blue LED was modulated with a 50% duty cycle square wave at 20 Hz, the green and red LEDs at 40 Hz, the NIR LED at 60 Hz, and the SWIR LED at 80 Hz, the OCF-OPD was set to detect NIR light. Upon activation, the device's response spectrum aligned with the output spectrum of the NIR light (Figure 5a). In contrast, when all sources were simultaneously activated with the same modulation as mentioned above, the commercial Si PD produced a chaotic waveform devoid of a consistent pattern (the bottom panel of Figure 5a).

To evaluate the device's reliability, we performed experiments with various signal outputs, including different waveforms, duty cycles, and frequencies, as illustrated in Figure S12 (Supporting Information). Results for modifications in one or two signals concerning duty cycles and waveforms are presented in Figures S13, S14 (Supporting Information). Our primary focus was on the OCF-OPD's capability to recognize NIR signals, comparing its performance to that of a commercial Si PD. The results demonstrate that the OCF-OPD exhibits robust anti-interference recognition capability, particularly in accurately identifying NIR signals amidst interference from red, green, blue, and SWIR light sources.

Building on this anti-interference signal recognition, we encoded specific information using the American Standard Code for Information Interchange (ASCII) into light signals. The results are shown in Figure 5b. The word "RAB" (representing "Rabbit") was encoded with visible light (green line), while "DRA" (representing "Dragon") was encoded with NIR light (red line). During anti-interference optical communication, the

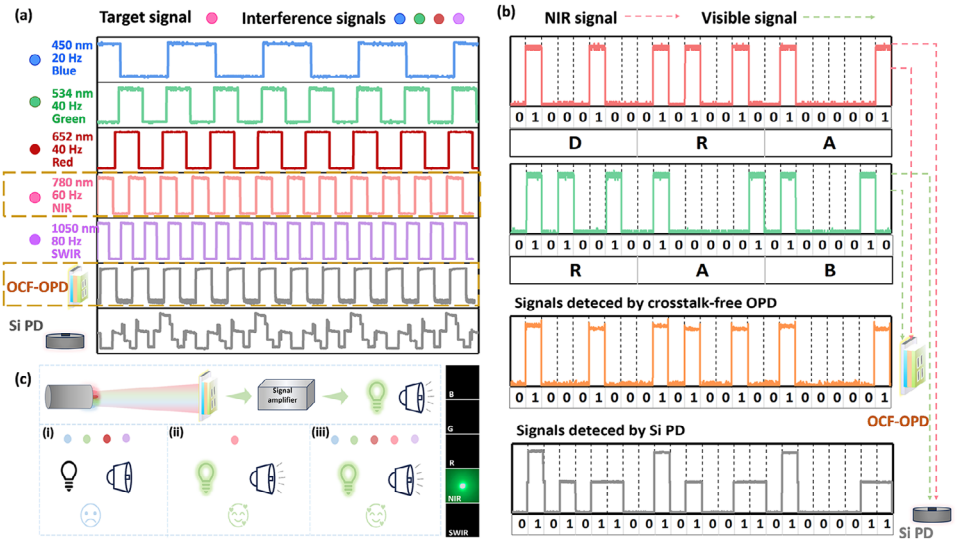

Figure 5. Demonstration of anti-interference optical communication using the OCF-OPDs. a) Signal detection performance of the OCF-OPD under modulated LEDs: blue (450 nm), green (534 nm), red (652 nm), NIR (780 nm), and SWIR (1050 nm). The outputs from the OCF-OPD are compared to a Si PD. b) ASCII-encoded light information transmitted as "DRA" (NIR signal) and "RAB" (visible light signal), recorded by a Si PD receiver and an OCF-OPD, respectively. The NIR signals are the target signals. c) Conceptual diagram of a simple encrypted communication application utilizing the OCF-OPD, showing its robust anti-interference and signal recognition capabilities. The target signal (represented in pink) is 780 nm.

wireless transmitter broadcasted light signals containing both "RAB" and "DRA." The broadband Si PD-based receiver captured the mixed signals of visible and NIR light (gray line), but the OCF-OPD successfully decoded the NIR-encoded signal "DRA" (orange line), while the visible light signal elicited no response.

Lastly, we introduced a simple demo for encrypted optical communication utilizing the OCF-OPD. By converting the electrical signal produced by the device into LED light and buzzer sound signals, a basic encrypted communication application was realized, as depicted in Figure 5c. In this setup, NIR light signals acted as keys, while blue, green, red, and SWIR signals served as interference. When only the blue, green, red, and SWIR lights were active, the LED remained off, and the buzzer was silent (see panel i in Figure 5c). However, when only the NIR light was active, or when it coexisted with the other lights, the LED emitted a vibrant green light (see panels ii-iii in Figure 5c; Video S1, Supporting Information), accompanied by buzzer activation (Video S2, Supporting Information). This demonstration showcased the OCF-OPD's robust anti-interference and signal recognition capabilities.

3. Conclusion

In summary, this study demonstrated a useful strategy for achieving optical crosstalk-free performance in dual-band OPDs through innovative integration of optical design and one-step transfer printing techniques. By utilizing a vertical stacking configuration, we place the BHJ-1 for visible light detection at the front and another BHJ-2 for NIR light at the rear. The one-step transfer printing method allows for increased thickness of the rear NIR absorbing BHJ, further filtering out undesired short-wavelength light and optimizing charge collection. This design successfully eliminates optical crosstalk between the two detection bands, resulting in an OCF-OPD with peak responsivities of 115.0 mA W^{-1} for visible light under forward bias and 85.5 mA W^{-1} for narrowband NIR light (FWHM < 50 nm) at reverse bias. The dual-band OPDs demonstrate exceptional capability in distinguishing target signals against interference, showcasing their potential for practical applications. These results not only tackle the issue of optical crosstalk in dual-band OPDs but also pave the way for future advancements in multi-band photodetector technologies.

4. Experimental Section

Materials: The donor polymers P3HT and PTB7-Th were sourced from Xi'an Polymer Light Technology Corp. and Organtec Ltd., respectively. The patterned ITO substrates and acceptors of PC_{61} BM and PC_{71} BM were obtained from Advanced Election Technology Co., Ltd., while Y6 was acquired from Organtec Ltd. All materials were used as received without further treatment. ZnO and MoO_3 nanoparticles were synthesized following a previously reported method.[43,44]

Device Fabrication: ITO substrates were cleaned ultrasonically in detergent, deionized water, ethanol, acetone, and isopropanol, followed by a 5-min UV-ozone treatment at 45 °C. ZnO nanoparticles were spin-coated onto the ITO/glass substrate at 2500 rpm for 35 s and annealed at 120 °C for 20 min. A P3HT:PC_{61} BM solution (2:1, 40 mg ml^{-1} in chlorobenzene) was then spin-coated on the ZnO layer and annealed at 120 °C for an additional 20 min. MoO_3 was subsequently spin-coated at 3000 rpm for 40 s and annealed at 120 °C for 10 min.

For the one-step transfer printing of rear BHJ, the pre-prepared PDMS substrate undergoes UV-ozone treatment (45 °C, 5 min) to remove surface impurities and adjust its surface energy. Next, a PTB7-Th:PC_{71} BM solution (1:1, 40 mg ml^{-1} in chlorobenzene) was spin-coated onto the UV-treated PDMS substrate at 2000 rpm for 30 s, forming a PDMS/PTB7-Th:PC_{71} BM film structure. The PTB7-Th:PC_{71} BM layer was then transferred onto the MoO_3 surface using a lamination technique and annealed at 100 °C for 10 min before removing the PDMS mold, resulting in the structure of ITO/ZnO/P3HT:PC_{61}BM/MoO_3/PTB7-Th:PC_{71}BM. ZnO nanoparticles were then deposited on the PTB7-Th:PC_{71} BM layer via spin-coating at 2000 rpm for 60 s and annealed at 120 °C for 20 min. Finally, a ≈130 nm

thick silver cathode was deposited in a vacuum chamber at a base pressure of 10^{-4} Pa.

Device Characterization: Absorption spectra were obtained using a UV-2600i spectrophotometer. *J-V* characteristics were recorded using a Keithley 2400 source meter. Transient photocurrent was recorded with various LED light sources, controlled by an AG1022E function generator. The responsivity of the OCF-OPD was evaluated with an EQE system, which included a QTEST HIFINITY 5 light source and a Stanford Research System SR830 lock-in amplifier. Noise spectral density was assessed using a Low-Frequency Noise Test System (LFN-1000, Wuxi Xinjian semiconductor-Tech Co,.Ltd). The photoresponse data were captured and amplified by a Tektronix MDO4024C oscilloscope and a VK40xD amplifier.

Supporting Information

Supporting Information is available from the Wiley Online Library or from the author.

Acknowledgements

This work was financially supported by the National Natural Science Foundation of China (11904298, 62305163), and the Venture and Innovation Support Program for Chongqing Overseas Returnees (cx2023063 and cx2024035). X.G. acknowledges the support of the Chongqing Municipal Training Program of Innovation and Entrepreneurship for Undergraduates (S202410635079).

Conflict of Interest

The authors declare no conflict of interest.

Data Availability Statement

The data that support the findings of this study are available from the corresponding author upon reasonable request.

Keywords

dual-band photodetection, narrowband, organic photodetectors, optical crosstalk, transfer printing technique

Received: January 8, 2025
Revised: February 27, 2025
Published online:

[1] Y. Wang, J. Kublitski, S. Xing, F. Dollinger, D. Spoltore, J. Benduhn, K. Leo, *Mater. Horiz.* **2022**, *9*, 220.
[2] X. Zhao, J. Wang, M. Liu, X. Ma, F. Zhang, *Adv. Opt. Mater.* **2024**, *12*, 2401087.
[3] Y. Hu, K. Wang, L. Chen, N. Li, Y. Lei, *The Innovation Mater.* **2024**, *2*, 100067
[4] T. Yan, Z. Li, F. Cao, J. Chen, L. Wu, X. Fang, *Adv. Mater.* **2022**, *34*, 2201303.
[5] A. Armin, R. D. Jansen-Van Vuuren, N. Kopidakis, P. L. Burn, P. Meredith, *Nat. Commun.* **2015**, *6*, 6343.
[6] J. Liu, J. Wang, K. Xian, W. Zhao, Z. Zhou, S. Li, L. Ye, *Chem. Commun.* **2022**, *59*, 260.
[7] V. Pejović, E. Georgitzikis, I. Lieberman, P. E. Malinowski, P. Heremans, D. Cheyns, *Adv. Funct. Mater.* **2022**, *32*, 2201424.
[8] H. Jiang, Y. Hu, H. Jiang, T. Wei, K. Wang, L. Chen, Q. Zhang, Y. Lei, *Adv. Funct. Mater.* **2025**, 2419686.
[9] S. J. Lim, D. S. Leem, K. B. Park, K. S. Kim, S. Sul, K. Na, G. H. Lee, C. J. Heo, K. H. Lee, X. Bulliard, R. I. Satoh, T. Yagi, T. Ro, D. Im, J. Jung, M. Lee, T. Y. Lee, M. G. Han, Y. W. Jin, S. Lee, *Sci. Rep.* **2015**, *5*, 7708.
[10] Q. Lin, A. Armin, P. L. Burn, P. Meredith, *Nat. Photonics* **2015**, *9*, 687.
[11] Y. Fang, Q. Dong, Y. Shao, Y. Yuan, J. Huang, *Nat. Photonics* **2015**, *9*, 679.
[12] L. Shen, Y. Fang, H. Wei, Y. Yuan, J. Huang, *Adv. Mater.* **2016**, *28*, 2043.
[13] W. Wang, F. Zhang, M. Du, L. Li, M. Zhang, K. Wang, Y. Wang, B. Hu, Y. Fang, J. Huang, *Nano Lett.* **2017**, *17*, 1995.
[14] W. Wang, M. Du, M. Zhang, J. Miao, Y. Fang, F. Zhang, *Adv. Opt. Mater.* **2018**, *6*, 1800249.
[15] M. S. G. Han, B. Park, J. Choi, S. Chung, D. Lee, K. Cho, *Adv. Opt. Mater.* **2024**, *12*, 2303308.
[16] M. Liu, J. Wang, Z. Zhao, K. Yang, P. Durand, F. Ceugniet, G. Ulrich, L. Niu, Y. Ma, N. Leclerc, X. Ma, L. Shen, F. Zhang, *J. Phys. Chem. Lett.* **2021**, *12*, 2937.
[17] B. Xie, R. Xie, K. Zhang, Q. Yin, Z. Hu, G. Yu, F. Huang, Y. Cao, *Nat. Commun.* **2020**, *11*, 2871.
[18] Z. Lan, Y. S. Lau, Y. Wang, Z. Xiao, L. Ding, D. Luo, F. Zhu, *Adv. Opt. Mater.* **2020**, *8*, 2001388.
[19] Z. Lan, Y. Lei, W. K. E. Chan, S. Chen, D. Luo, F. Zhu, *Sci. Adv.* **2020**, *6*, eaaw8065.
[20] Y. Gao, C. Zhao, K. Pu, M. He, W. Cai, M. C. Tang, F. Kang, H. L. Yip, G. Wei, *Sci. Bull.* **2022**, *67*, 1982.
[21] N. Li, N. Eedugurala, J. D. Azoulay, T. N. Ng, *Cell Rep. Phys. Sci.* **2022**, *3*, 100711.
[22] Z. Lan, Y. S. Lau, L. Cai, J. Han, C. W. Suen, F. Zhu, *Laser Photonics Rev.* **2022**, *16*, 2100602.
[23] C. Zou, D. Yu, M. Lin, B. Shen, Y. Peng, Y. Zheng, H. G. Yang, Y. Hou, S. Yang, *Adv. Funct. Mater.* **2024**, *34*, 2316430.
[24] R. D. Jansen-van Vuuren, A. Armin, A. K. Pandey, P. L. Burn, P. Meredith, *Adv. Mater.* **2016**, *28*, 4766.
[25] Z. Zhao, M. Liu, K. Yang, C. Xu, Y. Guan, X. Ma, J. Wang, F. Zhang, *Adv. Funct. Mater.* **2021**, *31*, 2106009.
[26] Z. Han, X. Liao, Y. Zou, Y. He, J. Li, Y. Gu, D. Hu, J. Liu, L. Zuo, Y. Liu, X. Xu, *ACS Nano* **2022**, *16*, 21036.
[27] H. Shekhar, A. Fenigstein, T. Leitner, B. Lavi, D. Veinger, N. Tessler, *Sci. Rep.* **2020**, *10*, 7594.
[28] T. Yan, Z. Li, L. Su, L. Wu, X. Fang, *Adv. Funct. Mater.* **2023**, *33*, 2302746.
[29] T. Yan, X. Liu, X. Zhang, E. Hong, L. Wu, X. Fang, *Adv. Funct. Mater.* **2024**, *34*, 2311042.
[30] Z. Lan, F. Zhu, *ACS Nano* **2021**, *15*, 13674.
[31] P. Wu, L. Ye, L. Tong, P. Wang, Y. Wang, H. Wang, H. Ge, Z. Wang, Y. Gu, K. Zhang, Y. Yu, M. Peng, F. Wang, M. Huang, P. Zhou, W. Hu, *Light Sci. Appl.* **2022**, *11*, 6.
[32] W. Hu, Z. Ye, L. Liao, H. Chen, L. Chen, R. Ding, L. He, X. Chen, W. Lu, *Opt. Lett.* **2014**, *39*, 5184.
[33] J. Zhao, X. Wang, Y. Xu, Y. Pan, Y. Li, J. Chen, Q. Li, X. Zhang, Z. Zhu, Z. Zhao, E. E. Elemike, D. C. Onwudiwe, B. S. Bae, S. Bin Shafie, W. Lei, *ACS Appl. Mater. Interfaces* **2022**, *14*, 25824.
[34] Y. Zhang, Z. Qin, X. Huo, D. Song, B. Qiao, S. Zhao, *ACS Appl. Mater. Interfaces* **2021**, *13*, 61818.
[35] N. Chander, S. Singh, S. S. K. Iyer, *Sol. Energy Mater. Sol. Cells* **2017**, *161*, 407.
[36] X. Fei, D. Jiang, M. Zhao, *Cryst. Growth Des.* **2023**, *23*, 1559.
[37] E. T. Simola, A. De Iacovo, J. Frigerio, A. Ballabio, A. Fabbri, G. Isella, L. Colace, *Opt. Express.* **2019**, *27*, 8529.
[38] L. Cui, Y. Tang, Q. Zhu, J. Luo, S. Hu, *Acta Phys. Sin.* **2016**, *65*, 094208.
[39] F. Alishahi, A. Mohajerin-Ariaei, A. Fallahpour, Y. Cao, A. Almaiman, P. Liao, C. Bao, B. Shamee, K. Zou, H. Zhou, A. N. Willner, J. D. Touch,

M. Tur, C. Langrock, M. M. Fejer, A. E. Willner, *J. Lightwave Technol.* **2019**, *37*, 548.
[40] T. Bills, C.-T. Liu, J. Lim, N. Eedugurala, P. Mahalingavelar, B. Seo, E. T. Hanna, T. N. Ng, J. D. Azoulay, *Adv. Funct. Mater.* **2024**, *34*, 2314210.
[41] Z. Lan, M.-H. Lee, F. Zhu, *Adv. Intell. Syst.* **2022**, *4*, 2100167.
[42] K. Wang, Y. Hu, L. Chen, H. Jiang, H. Jiang, X. Tan, Q. Zhang, Y. Lei, *Appl. Phys. Lett.* **2024**, *125*, 113302.
[43] J. Kwak, W. K. Bae, D. Lee, I. Park, J. Lim, M. Park, H. Cho, H. Woo, D. Y. Yoon, K. Char, S. Lee, C. Lee, *Nano Lett.* **2012**, *12*, 2362.
[44] X. Li, W. C. H. Choy, F. Xie, S. Zhang, J. Hou, *J. Mater. Chem. A* **2013**, *1*, 6614.